AIAA JOURNAL
Vol. 60, No. 7, July 2022

Effect of Yaw Angle on Flutter of Rectangular Plates at Low Supersonic Speeds

Farrukh A. Abdukhakimov* and Vasily V. Vedeneev†
Lomonosov Moscow State University, 119992, Moscow, Russia

https://doi.org/10.2514/1.J061441

The stability of the infinite series of thin elastic rectangular plates simply supported along all edges and exposed to a supersonic flow is investigated. The nonzero flow yaw angle with supersonic leading edge is considered. To derive expression for the unsteady aerodynamic pressure distribution over the oscillating plate, potential flow theory was used, and an integrodifferential eigenvalue problem for finding complex eigenvalues was obtained. Flutter boundaries for the first and second modes are computed. Changing of the single-mode and coupled-mode flutter boundaries with the change of the yaw angle was shown. While they are smooth at zero angle, the boundaries become irregular, and additional isolated regions of stability and instability appear when increasing the yaw angle. This irregularity occurs due to the interaction of multiple spanwise modes, which takes place at nonzero yaw angle due to their aerodynamic coupling.

Nomenclature

a_0	=	freestream speed of sound
D	=	dimensionless stiffness of the plate, $D_w/(a_0^2\rho_m h^3)$
D_w	=	dimensional stiffness of the plate, $(\mathrm{kg}\cdot\mathrm{m}^2)/\mathrm{s}^2$
h	=	plate thickness, m
I	=	identity matrix
k, l	=	number of half-waves in the x and y directions
L_x	=	plate length
L_y	=	plate width
M	=	Mach number
N_x, N_y	=	number of basic modes
P	=	aerodynamic matrix
p	=	pressure perturbation
K	=	diagonal stiffness matrix, which represents the plate properties
S	=	triangle that is an intersection of the plate and the reversed Mach cone with the vertex at the point (ξ, η)
t	=	time
U_0	=	gas flow speed, Ma_0, m/s
w	=	plate deflection
x, y, z	=	spatial coordinates
Δ	=	Laplace operator
ε	=	value of the relative inaccuracy
η	=	spatial coordinate
θ	=	flow yaw angle
κ	=	wave number, $\pi k/L_x$
λ	=	wave number, $\pi l/L_y$
μ	=	gas density, ρ_0/ρ_m
ξ	=	spatial coordinate
ρ_m	=	plate material density, $\mathrm{kg/m}^3$
ρ_0	=	gas density, $\mathrm{kg/m}^3$
φ	=	flow potential
ω	=	complex eigenvalue
ω_n	=	nth eigenvalue

I. Introduction

WHEN aircraft skin panels interact with the air flow at high flight speeds, loss of stability and intense vibrations of skin panels, known as the phenomenon of panel flutter, may occur. Usually this phenomenon leads to the accumulation of fatigue damage of the panels, followed by their destruction [1]. The first type of the panel flutter, the coupled-mode flutter, occurs due to the interaction of two oscillation eigenmodes. The coupled-mode flutter has been studied in detail using the piston theory [1–5], which is suitable as an aerodynamic model at high supersonic speeds ($M > 2$). The second type of panel flutter, the single-mode flutter, is caused by negative aerodynamic damping. In this case, the coalescence of eigenfrequencies and a significant change in the oscillation mode shape do not take place. The single-mode flutter arises at a low supersonic speed, where the piston theory is inapplicable, and therefore it is necessary to use more general aerodynamic models [6–14].

Most of panel flutter studies consider either cylindrical shells [15,16] or rectangular plates and, rarely, skewed plates or other forms with the flow perpendicular to the leading edge [17,18]. Also, there are a number of recent studies of curved panels [19,20]. Only a few works [21–23] investigate panel flutter at the nonzero yaw angle. However, they used the piston theory or its modifications, which are applicable only at high Mach numbers. For Mach numbers $M < 2$, the piston theory becomes invalid and incapable to predict single-mode flutter that exists at low supersonic speeds. Therefore, in this range of flow parameters it is necessary to use more general aerodynamic models. In Ref. [24], the flutter boundaries for isolated rectangular plate and infinite series of rectangular plates are studied using potential flow theory; zero yaw angle was considered. The present paper develops the analysis method of Ref. [24] and presents calculated results for the case of nonzero flow yaw angle.

The structure of the paper is as follows: Section I gives the problem statement and briefly describes the calculation method. In Sec. II the expression for the pressure perturbation is derived. Section III presents a convergence study, and Sec. IV discusses the results of this work. Finally, in Sec. V, conclusions are given.

II. Problem Formulation and Method of Solution

The stability of the infinite series of thin elastic rectangular plates, of length L_x and width L_y, at nonzero flow yaw angle θ is investigated (Fig. 1). Each plate is simply supported along all edges. One side of the plate surface is exposed to a homogeneous supersonic flow of perfect inviscid gas. Supersonic leading edge ($M\cos\theta > 1$) is considered.

Let us introduce two coordinate systems xyz and $\xi\eta z$ as shown in Fig. 1. The gas flows along the ξ axis, whereas the η axis is directed across the flow, and the z axis is normal to the plate surface. One side of the plate is directed along the x axis, whereas the other along the y axis.

Received 8 November 2021; revision received 1 February 2022; accepted for publication 2 February 2022; published online 28 February 2022.

*Junior Researcher, Institute of Mechanics; afa_mech@mail.ru.
†Head of Laboratory, Institute of Mechanics.

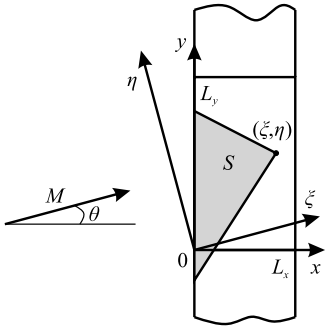

Fig. 1 Flow over a series of plates. Triangle S is shown in gray.

Assuming homogeneous unperturbed flow and adiabatic motion of the gas, the perturbed flow is necessarily potential. In the $\xi\eta z$ coordinates, the dimensionless flow equations (1–3) and expression for the pressure perturbation over the plate, Eq. (4), have the form:

$$\frac{\partial^2\varphi}{\partial t^2} + 2M\frac{\partial^2\varphi}{\partial\xi\partial t} + (M^2-1)\frac{\partial^2\varphi}{\partial\xi^2} - \frac{\partial^2\varphi}{\partial\eta^2} - \frac{\partial^2\varphi}{\partial z^2} = 0 \tag{1}$$

$$\left.\frac{\partial\varphi}{\partial z}\right|_{z=0} = \frac{\partial w}{\partial t} + M\frac{\partial w}{\partial\xi} \tag{2}$$

$$\left(\frac{\partial\varphi}{\partial\xi}, \frac{\partial\varphi}{\partial\eta}, \frac{\partial\varphi}{\partial z}\right) \to 0 \text{ as } z \to +\infty \text{ along characteristics } z = \frac{\xi-\xi_0}{\sqrt{M^2-1}} \tag{3}$$

$$p = -\mu\left(\frac{\partial}{\partial t} + M\frac{\partial}{\partial\xi}\right)\varphi(\xi,\eta,0,t)$$
$$\varphi = \varphi(\xi,\eta,z,t), w = w(\xi,\eta,t), p = p(\xi,\eta,t) \tag{4}$$

where φ, t, w, p, M, and μ are dimensionless flow potential, time, plate deflection, pressure perturbation, Mach number, and gas density, respectively.

For nondimensionalization, the plate thickness h, freestream speed of sound a_0, and plate material density ρ_m are used as independent scales. Hence, dimensional quantities (denoted by a prime) are expressed as $\varphi' = \varphi a_0 h$, $U_0 = M a_0$, $\xi' = \xi h$, $\eta' = \eta h$, $z' = zh$, $t' = th/a_0$, $w' = wh$, $p' = \rho_m a_0^2 p$, $\rho_0 = \mu\rho_m$.

Small perturbations are considered in the form

$$\varphi(\xi,\eta,z,t) = \Phi(\xi,\eta,z)e^{-i\omega t}, w(\xi,\eta,t) = W(\xi,\eta)e^{-i\omega t}, p(\xi,\eta,t) = \Pi(\xi,\eta)e^{-i\omega t} \tag{5}$$

where ω is complex eigenvalue. Substitution into Eqs. (1–4) yields

$$-\omega^2\Phi - 2i\omega M\frac{\partial\Phi}{\partial\xi} + (M^2-1)\frac{\partial^2\Phi}{\partial\xi^2} - \frac{\partial^2\Phi}{\partial\eta^2} - \frac{\partial^2\Phi}{\partial z^2} = 0 \tag{6}$$

$$\left.\frac{\partial\Phi}{\partial z}\right|_{z=0} = -i\omega W + M\frac{\partial W}{\partial\xi} \tag{7}$$

$$\Pi = -\mu\left(-i\omega + M\frac{\partial}{\partial\xi}\right)\Phi(\xi,\eta,0) \tag{8}$$

The solution of the system of Eqs. (6–8) is as follows [25]:

$$\Phi(\xi,\eta,0) = -\frac{1}{\pi}\iint_S\left(-i\omega W(\xi_1,\eta_1) + M\frac{\partial W(\xi_1,\eta_1)}{\partial\xi}\right) \times \exp\left(\frac{i\omega M}{\beta^2}(\xi-\xi_1)\right) \times \frac{\cos\left(\frac{\omega}{\beta^2}\sqrt{(\xi-\xi_1)^2-\beta^2(\eta-\eta_1)^2}\right)}{\sqrt{(\xi-\xi_1)^2-\beta^2(\eta-\eta_1)^2}}d\xi_1 d\eta_1 \tag{9}$$

where $\beta = \sqrt{M^2-1}$, and S is a triangle that is an intersection of the plate and the reversed Mach cone with the vertex at the point (ξ,η) (Fig. 1).

Linear Kirchhoff–Love plate theory is used; in-plane tension of the plate is neglected. In the x,y coordinates the plate equation and boundary conditions have the form

$$D\Delta^2 W(x,y) - \omega^2 W(x,y) + \Pi(x,y) = 0 \tag{10}$$

$$W(x,y) = \frac{\partial^2 W(x,y)}{\partial x^2} = 0, x = 0, L_x \tag{11}$$

$$W(x,y) = \frac{\partial^2 W(x,y)}{\partial y^2} = 0, y = 0, L_y \tag{12}$$

where Δ is the two-dimensional Laplace operator, $D = D_w/(a_0^2\rho_m h^3)$, and D_w are dimensionless and dimensional bending stiffness of the plate, respectively. In Eq (10), pressure perturbation $\Pi(x,y)$ is given in coordinate system xyz, which is associated with the plate.

Equations (8) and (9) and transformation of coordinates are used to get the expression for the pressure perturbation in xyz coordinates. After the substitution of this expression, the plate equation (10) with simply supported boundary conditions (11) and (12) is an integro-differential eigenvalue problem for finding eigenvalues ω. The calculation method is described in detail in Ref. [24]; its essence is as follows. Eigenvalue problem is solved numerically using the Bubnov–Galerkin procedure. The plate deflection is expressed as a superposition of the plate mode shapes in vacuum:

$$W(x,y) = \sum_{k=1}^{N_x}\sum_{l=1}^{N_y} C_l^k W_k(x) W^l(y) = \sum_{k=1}^{N_x}\sum_{l=1}^{N_y} C_l^k \sin(\varkappa x)\sin(\lambda y),$$
$$\varkappa = \frac{\pi k}{L_x}, \lambda = \frac{\pi l}{L_y} \tag{13}$$

This leads to the equation for complex eigenvalues:

$$\det\left(K - \frac{L_x\omega^2}{2}I + P(\omega)\right) = 0 \tag{14}$$

where I is the identity matrix; K is the diagonal stiffness matrix, which represents the plate properties; and P is aerodynamic matrix, whose elements are calculated as

$$p_{mn} = \frac{2}{L_y}\int_0^{L_x}\int_0^{L_y}\Pi(x,y,T_n,\omega)T_m(x,y)\,dx\,dy,$$
$$T_i = \sin\left(\frac{k\pi x}{L_x}\right)\sin\left(\frac{l\pi y}{L_y}\right), l = \left[\frac{i-1}{N_x}\right] + 1, k = i - N_x(l-1) \tag{15}$$

The frequency equation is solved by the iterative method [24]. Iterations for n th eigenfrequency ω_n are continued until the relative inaccuracy becomes sufficiently small:

$$\left|\frac{\omega_{np} - \omega_{n,p-1}}{\omega_{np}}\right| < \varepsilon \tag{16}$$

where ω_{np}, $\omega_{n,p-1}$ are the values of the n th eigenfrequency at the pth and $(p-1)$th iteration steps.

The positive sign of $\mathrm{Im}\omega_n$ is the flutter criterion.

Since linear Kirchhoff–Love plate theory is used, only flutter boundaries are studied, and postflutter behavior and limit cycles of oscillations are not considered.

Compared to Ref. [24], the difference of the present study is in the calculation of aerodynamic matrix due to the nonzero yaw angle. The next section describes the details of the aerodynamic matrix calculation.

III. Distribution of Pressure Disturbance over the Plate

Let us obtain an expression for the pressure perturbation acting on the plate in the coordinate system xyz associated with the plate. The transformation of coordinates has the form

$$\xi = x\cos\theta + y\sin\theta, \eta = -x\sin\theta + y\cos\theta$$
$$\frac{\partial}{\partial\xi} = \frac{\partial}{\partial x}\frac{\partial x}{\partial\xi} + \frac{\partial}{\partial y}\frac{\partial y}{\partial\xi} = \frac{\partial}{\partial x}\cos\theta + \frac{\partial}{\partial y}\sin\theta \tag{17}$$

If $W(x, y)$ is considered in the form

$$W(x, y) = W(x)e^{i\lambda y} \tag{18}$$

then multipliers of the integrand in Eq. (9) are transformed as

$$-i\omega W(\xi_1, \eta_1) + M\frac{\partial W(\xi_1, \eta_1)}{\partial\xi} = \left(-i(\omega - \lambda M_y)W(x_1) + M_x\frac{\partial W(x_1)}{\partial x_1}\right)e^{i\lambda y_1} \tag{19}$$

$$\exp\left(\frac{i\omega M}{\beta^2}(\xi - \xi_1)\right) = \exp\left(\frac{i\omega M_x}{\beta^2}(x - x_1)\right)\exp\left(\frac{i\omega M_y y}{\beta^2}\right) \times \exp\left(-\frac{i\omega M_y y_1}{\beta^2}\right) \tag{20}$$

and expression under the square root is modified to the form:

$$(\xi - \xi_1)^2 - \beta^2(\eta - \eta_1)^2 = (x - x_1)^2\frac{\beta^2}{M_x^2 - 1} - (M_x^2 - 1)\left[y_1 - \left(y - \frac{(x - x_1)M_x M_y}{M_x^2 - 1}\right)\right]^2 \tag{21}$$

where $M_x = M\cos\theta$ and $M_y = M\sin\theta$.

The integration limits in the xyz coordinate system are

$$y_{1b} = \frac{(x - x_1)(\cos\theta - \beta\sin\theta)}{\beta\cos\theta + \sin\theta} + y \tag{22}$$

$$y_{1a} = -\frac{(x - x_1)(\cos\theta + \beta\sin\theta)}{\beta\cos\theta - \sin\theta} + y \tag{23}$$

Integrating Eq. (9) by parts and calculating integral over y in a closed form, we obtain the expression for the potential in the xy coordinate in the form

$$\Phi(x, y, 0) = -\frac{e^{\mathrm{iky}}}{\sqrt{M_x^2 - 1}}\int_0^x\left(-i(\omega - \lambda M_y)W(x_1) + M_x\frac{\partial W(x_1)}{\partial x_1}\right)J_{0,1}e^{A_1(x - x_1)}\mathrm{d}x_1 \tag{24}$$

where $J_{0,1} = J_0(B_1(x - x_1))$, J_0 is zero-order Bessel function of the first kind:

$$A_1 = iM_x(\omega - \lambda M_y)/(M_x^2 - 1),$$

and

$$B_1 = \frac{\sqrt{\lambda^2(M_x^2 - 1) + (\omega - \lambda M_y)^2}}{M_x^2 - 1}$$

Therefore, the following pressure perturbation for $W(x, y) = W(x)e^{i\lambda y}$ is obtained:

$$\Pi_1(x, y) = -\mu\left(-i\omega + M_x\frac{\partial}{\partial x} + M_y\frac{\partial}{\partial y}\right)\Phi(x, y, 0) = \tilde{\Pi}_1(x)e^{i\lambda y} \tag{25}$$

$$\tilde{\Pi}_1(x) = \frac{\mu M_x}{\sqrt{M_x^2 - 1}}\left(-i(\omega - \lambda M_y)W(x) + M_x\frac{\partial W(x)}{\partial x}\right) + \frac{\mu}{(\sqrt{M_x^2 - 1})^3}\int_0^x\left(i(\omega - \lambda M_y)J_{0,1} - M_x J_{1,1}\sqrt{\lambda^2(M_x^2 - 1) + (\omega - \lambda M_y)^2}\right) \times\left(-i(\omega - \lambda M_y)W(x_1) + M_x\frac{\partial W(x_1)}{\partial x_1}\right)e^{A_1(x - x_1)} \tag{26}$$

where $J_{1,1} = J_1(B_1(x - x_1))$, J_1 is first-order Bessel function of the first kind.

For the plate deflection $W(x, y)$ given in the form

$$W(x, y) = W(x)e^{-i\lambda y} \tag{27}$$

similarly, the expression for the potential $\Phi(x, y, 0)$ and pressure disturbance

$$\Pi_2(x, y) = \tilde{\Pi}_2(x)e^{-i\lambda y} \tag{28}$$

are obtained by simply changing the sign of λ:

$$\tilde{\Pi}_2(x) = \frac{\mu M_x}{\sqrt{M_x^2 - 1}}\left(-i(\omega + \lambda M_y)W(x) + M_x\frac{\partial W(x)}{\partial x}\right) + \frac{\mu}{(\sqrt{M_x^2 - 1})^3}\int_0^x\left(i(\omega + \lambda M_y)J_{0,2} - M_x J_{1,2}\sqrt{\lambda^2(M_x^2 - 1) + (\omega + \lambda M_y)^2}\right) \times\left(-i(\omega + \lambda M_y)W(x_1) + M_x\frac{\partial W(x_1)}{\partial x_1}\right)e^{A_2(x - x_1)}\mathrm{d}x_1 \tag{29}$$

where $J_{0,2} = J_0(B_2(x - x_1))$, $J_{1,2} = J_1(B_2(x - x_1))$,

$$A_2 = i\frac{M_x(\omega + \lambda M_y)}{M_x^2 - 1}$$

and

$$B_2 = \frac{\sqrt{\lambda^2(M_x^2 - 1) + (\omega + \lambda M_y)^2}}{M_x^2 - 1}$$

Accordingly, the expression for the pressure perturbation for

$$W(x, y) = W(x)\sin(\lambda y) = W(x)\frac{e^{i\lambda y} - e^{-i\lambda y}}{2i} \tag{30}$$

is calculated as follows:

$$\tilde{\Pi}(x, y) = \frac{\tilde{\Pi}_1(x, y) - \tilde{\Pi}_2(x, y)}{2i} \tag{31}$$

The final expression of Eq. (31) is used below for calculation of the pressure matrix coefficients in Eq. (14).

The outer, Eq. (15), and inner, Eqs. (26) and (29), integrals are calculated by the trapezoidal method. When calculating the outer integral over x and y, the integration steps are

$$\Delta_x = \frac{L_x}{qN_x}, \Delta_y = \frac{L_y}{qN_y} \tag{32}$$

and to calculate the inner integral, a step is taken r times less than Eq. (32), where q and r are two refinement parameters.

IV. Convergence Study

To determine the parameters of the numerical calculation, first, the convergence was investigated. Plates with $L_y = 200$, 500, and 1000 were considered. Calculations were performed at yaw angles $\theta = 5$, 15, and 30°.

First, the convergence in the number of basic modes N_x and N_y was considered. The results are shown in Figs. 2 and 3; here, relative inaccuracy δ is defined as (similar definitions are used for other parameters of the numerical method) follows:

$$\delta_{Re}(N_x) = \left|\frac{Re\omega(N_x) - Re\omega(N_x - 1)}{Re\omega(N_x)}\right|,$$
$$\delta_{\mathrm{Im}}(N_x) = \left|\frac{\mathrm{Im}\omega(N_x) - \mathrm{Im}\omega(N_x - 1)}{\mathrm{Im}\omega(N_x)}\right| \tag{33}$$

$$\delta_{Re}(N_y) = \left|\frac{Re\omega(N_y) - Re\omega(N_y - 1)}{Re\omega(N_y)}\right|,$$
$$\delta_{\mathrm{Im}}(N_y) = \left|\frac{\mathrm{Im}\omega(N_y) - \mathrm{Im}\omega(N_y - 1)}{\mathrm{Im}\omega(N_y)}\right| \tag{34}$$

The range of chordwise number N_x from 2 to 12 and the range of spanwise number N_y from 1 to 6 are considered. It is clear that $N_x = 6$ and $N_y = 4$ give a satisfactorily converged results. Note that the number of basic functions required for the convergence is larger than in the case with zero yaw angle [24], which is caused by the interaction of higher spanwise modes that were uncoupled at zero yaw angle.

Next, the convergence of the solution was considered with respect to the value of the relative inaccuracy ε, Eq. (16); number of integration points q of the outer integral, per the shortest half-wave, Eq. (15); and the ratio of the external, Eq. (15), and internal, Eqs. (26) and (29), integration steps, r.

Calculations have shown that the results are converged at $\varepsilon \le 10^{-4}$ (Fig. 4). Therefore, $\varepsilon = 10^{-4}$ is enough for accurate calculations.

Figures 5 and 6 show the convergence of real and imaginary parts of the first two frequencies and their relative inaccuracies in q and r. As a result, $q = 6$ and $r = 3$ are chosen, which yields satisfactory accuracy. Note that the values of ε, q, and r sufficient to obtain accurate results are the same as when calculating at zero yaw angle.

Based on the convergence study, the following parameters of the numerical method are chosen: $N_x = 6$, $N_y = 4$, $\varepsilon = 10^{-4}$, $q = 6$, and $r = 3$. These values are used below in calculations of the panel flutter boundaries.

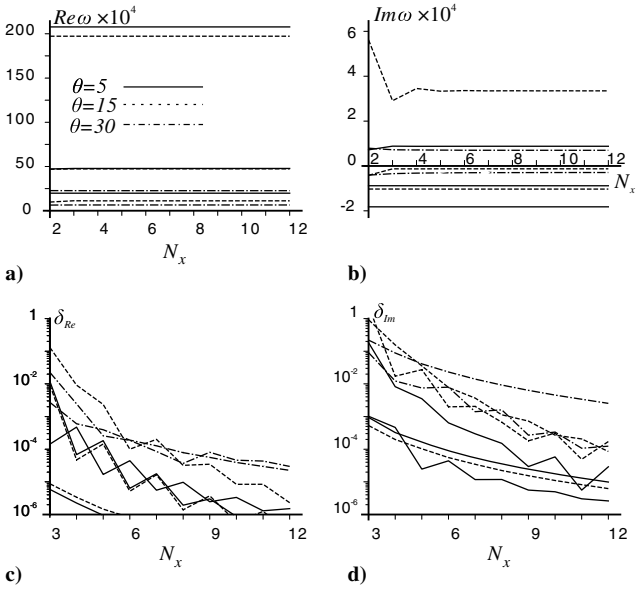

Fig. 2 Convergence in the chordwise number of basic modes N_x for the two first eigenmodes. $N_y = 2$, $\varepsilon = 10^{-6}$, $q = 10$, $r = 3$. Real a) and imaginary b) parts of the complex frequency and relative inaccuracies c, d) versus N_x.

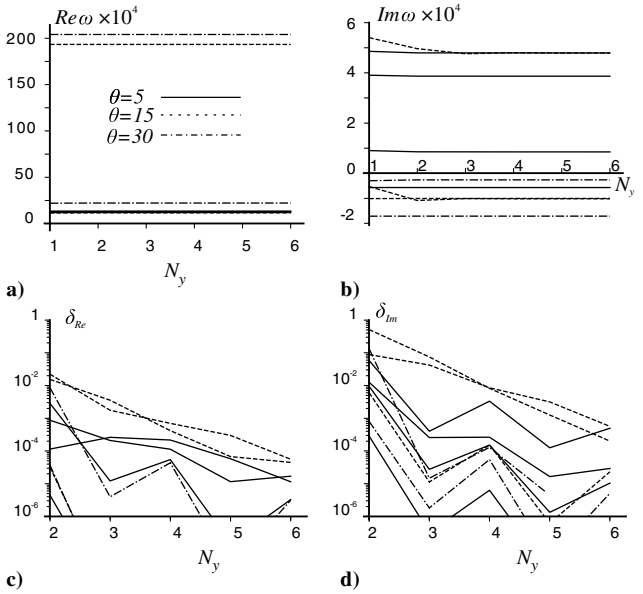

Fig. 3 Convergence in the spanwise number of basic modes N_y for the two first eigenmodes. $N_x = 6$, $\varepsilon = 10^{-6}$, $q = 10$, $r = 3$. Real a) and imaginary b) parts of the complex frequency and relative inaccuracies c, d) versus N_y.

V. Results

Panel flutter analysis of a series of rectangular plates with various sizes was conducted. The first ($k = 1$, $l = 1$) and the second ($k = 2$,

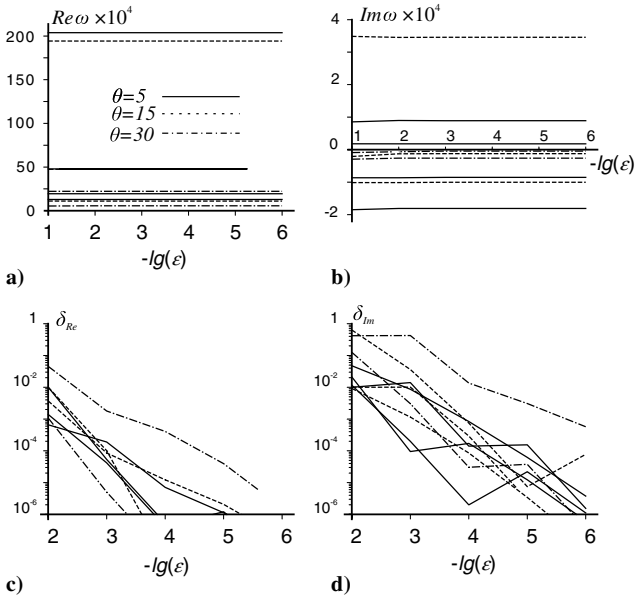

Fig. 4 Convergence in the relative inaccuracyε for the two first eigenmodes. $N_x = 6$, $N_y = 4$, $q = 10$, $r = 3$. Real a) and imaginary b) parts of the complex frequency and corresponding relative inaccuracies c, d) versus ε.

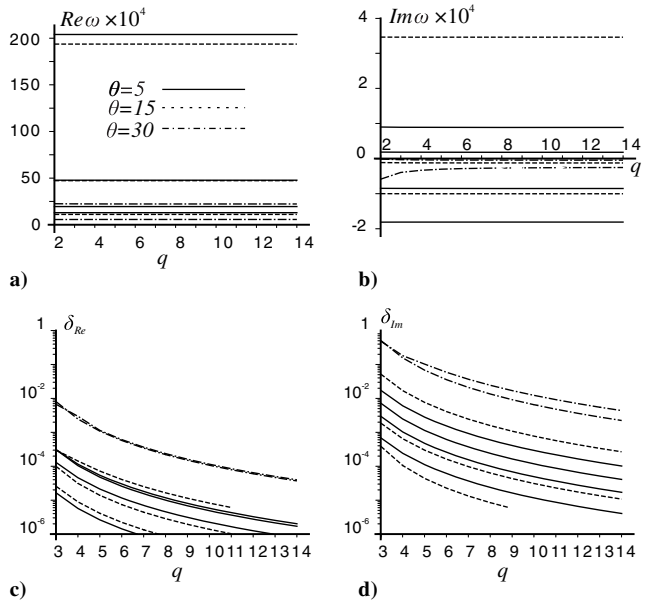

Fig. 5 Convergence in the number of integration points q of the outer integral per the shortest half-wave for the two first eigenmodes. $N_x = 6$, $N_y = 4$, $\varepsilon = 10^{-4}$, $r = 3$. Real a) and imaginary b) parts of the complex frequency and relative inaccuracies c, d) versus q.

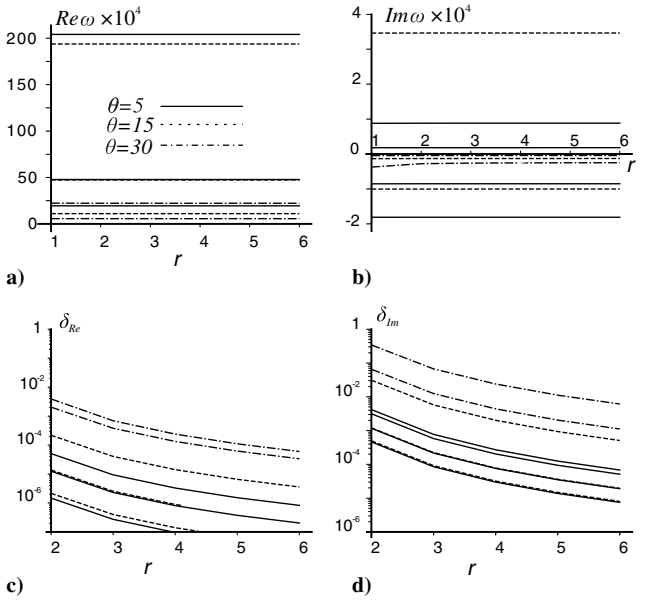

Fig. 6 Convergence in the ratio of the external and internal integration steps r for the two first eigenmodes. $N_x = 6$, $N_y = 4$, $\varepsilon = 10^{-4}$, $q = 6$. Real a) and imaginary b) parts of the complex frequency and relative inaccuracies c, d) versus r.

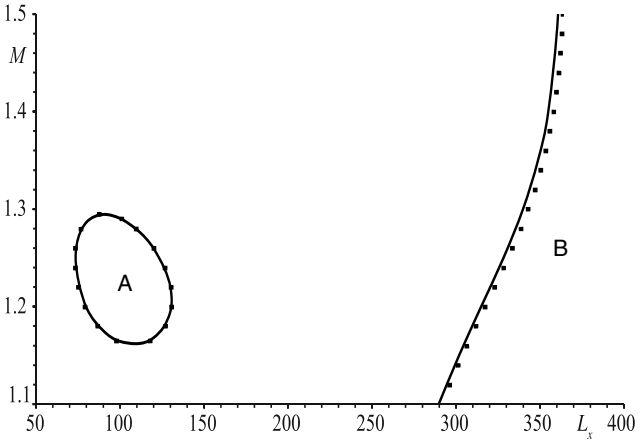

Fig. 7 Comparison of the results of this work (points) and the results of Shitov and Vedeneev [24] at zero yaw angle for the first mode and $L_y = 350$.

$l = 1$) plate modes are considered. The calculations were performed for the yaw angle $\theta = 0, 5, 10, 15, 20, 25$, and 30°. Investigation has been conducted at M from 1.05 to 1.7; at each value of θ the minimum Mach number was limited by the condition of supersonic leading edge ($M \cos\theta > 1$); otherwise, the integration region K is not finite, and the solution, Eq. (9), for the unsteady potential is not valid.

A. First-Mode Flutter

First, the case of zero yaw angle is considered. Figure 7 shows a comparison with the results obtained by Shitov and Vedeneev [24]. In Fig. 7 (as well as in Figs. 8–12 and 14–23), Mach number is plotted at the vertical axis, and dimensionless plate length at the horizontal axis. The solid line denotes the boundaries calculated by Shitov and Vedeneev [24], and the points denote the results of the present work. The isolated instability region on the left-hand side (A) corresponds to the single-mode flutter, whereas the unbounded region (B) represents coupled-mode flutter. The comparison of flutter boundaries shows that the results are in good agreement with each other.

Consider panel flutter boundaries at nonzero yaw angle. Results at $\theta = 5°$ for several L_y are shown in Fig. 8. The regions shaded with gray are the instability regions in the corresponding mode.

It is seen that the results are qualitatively close to the case of $\theta = 0°$ [24]. For $L_y = 1000$ and $L_x > 61$ there exists a segment of M in which the first mode flutter occurs. At $L_x \le 61$, the series of plates is stable with respect to the first mode. When L_y decreases, there is narrowing (in terms of Mach numbers) of the flutter region. For example, at $L_x = 280$, the series of plates is unstable at $1.1 \le M < 1.32$ for $L_y = 600$, and at $1.1 \le M < 1.24$ for $L_y = 460$. Below a certain value of L_y, the region of the instability is divided into a finite-size single-mode flutter region (region A at lower L_x) and a coupled flutter region B unbounded as $L_x \to \infty$. For instance, the isolated region of single-mode flutter exists at $60 < L_x < 198$ and $1.11 < M < 1.34$ for $L_y = 450$, and at $79 < L_x < 110$ and $1.19 < M < 1.28$ for $L_y = 340$, whereas coupled mode flutter in the first mode occurs at $L_x > 238$ for $L_y = 450$ and at $L_x > 305$ for $L_y = 340$. When

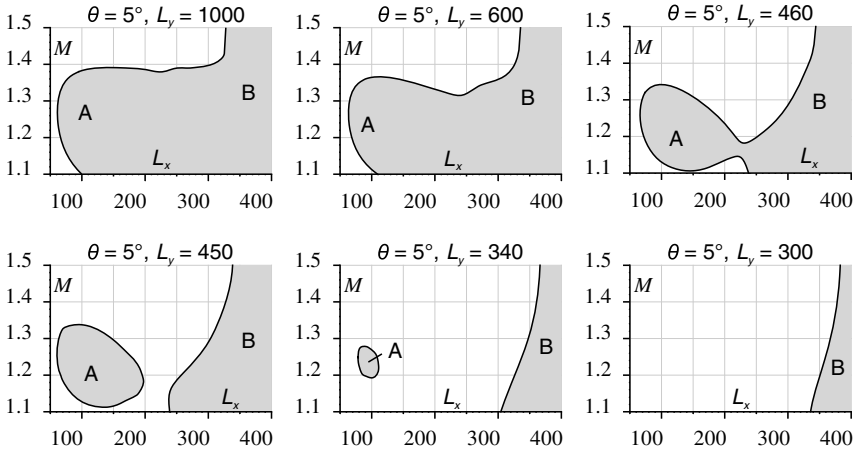

Fig. 8 Flutter boundaries for the first mode at $\theta = 5°$. The instability regions are shaded with gray.

lowering L_y, the single-mode flutter region contracts to a point and disappears, whereas the boundary of the coupled flutter is shifted to larger L_x. Figure 8 shows that for $L_y = 300$, coupled mode flutter takes place for $L_x > 335$.

With an increase of the yaw angle, the result becomes somewhat more complicated. Some irregularity appears in the instability boundaries. For large values of the width and for the length greater than a certain value, there is also a segment of Mach numbers, for which there is a panel flutter in the first mode. Namely, for $\theta = 10$ and $15°$ and $L_y = 1000$ the instability appears at $L_x > 60$. Further, with decreasing L_y, on one hand, narrowing of the unstable Mach number range takes place; on the other hand, additional regions of instability appear (region C in Fig. 9 and regions C–E in Fig. 10).

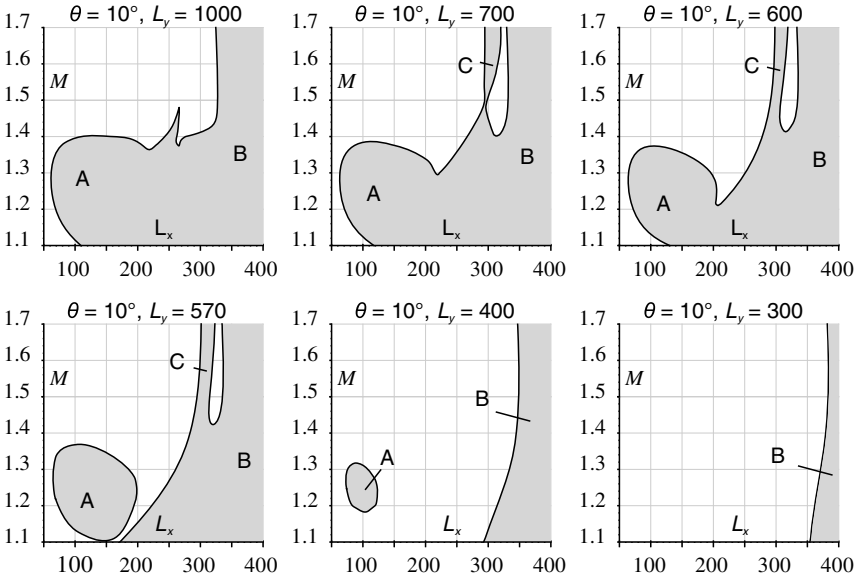

Fig. 9 Flutter boundaries for the first mode at $\theta = 10°$. The instability regions are shaded with gray.

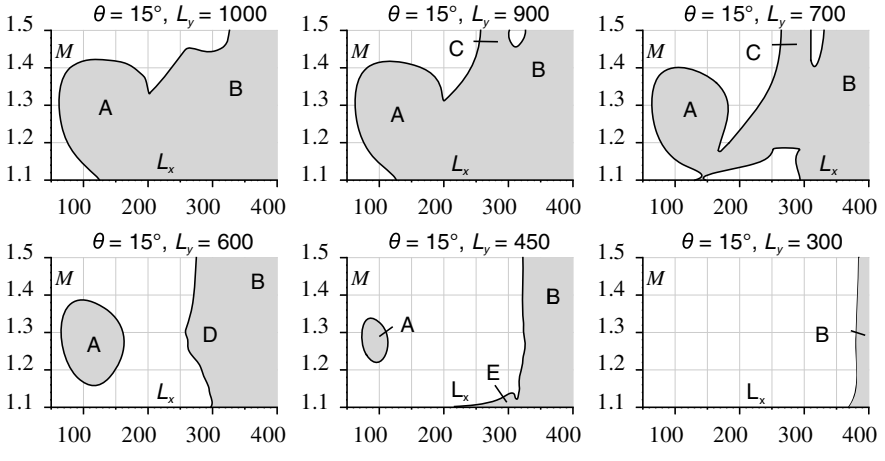

Fig. 10 Flutter boundaries for the first mode at $\theta = 15°$. The instability regions are shaded with gray.

As well as for smaller yaw angles, when decreasing L_y, the single-mode flutter region first becomes isolated, then reduces in size, contracts to a point, and finally disappears. Figure 9 shows that for $\theta = 10°$, the $L_y = 570$, isolated region of single-mode flutter appears at $65 < L_x < 200$ and $1.1 < M < 1.37$ and for $L_y = 400$ at $71 < L_x < 125$ and $1.18 < M < 1.32$. For $\theta = 15°$, the isolated region of single-mode flutter occurs at $65 < L_x < 165$ and $1.16 < M < 1.39$ for $L_y = 600$ and at $71 < L_x < 115$ and $1.22 < M < 1.34$ for $L_y = 450$. Below a certain value of L_y, the additional region caused by the interaction of three or more modes also disappears. In addition, the boundary of the coupled-mode flutter is shifted to larger L_x. Figure 9 shows that for $L_y = 300$ coupled mode flutter takes place at $L_x > 353$ for $\theta = 10°$ and at $L_x > 369$ for $\theta = 15°$. The value of L_y at which the single-mode flutter region disappears increases with increasing yaw angle: this critical value of the plate width is equal to 313, 324, 350, and 410 at $\theta = 0$, 5, 10, and 15°, respectively.

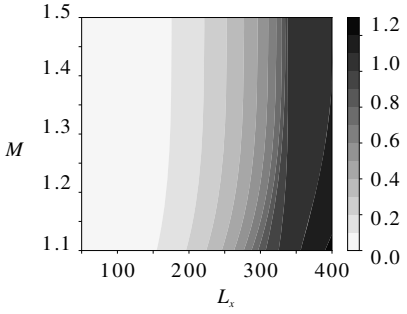

Fig. 11 Coefficients of the plate deflection expansion in natural mode shapes $|C_1^2|$ ($\theta = 0°$, $L_y = 600$).

To identify the mechanism of flutter, the expansion coefficients of the plate deflection in natural mode shapes, Eq. (13), with the condition that the first natural mode shape amplitude $C_1^1 = 1$, are calculated to determine which of the modes dominates in flutter oscillations (Fig. 11). At zero and small angles, the first mode dominates at low L_x, and so this is a single-mode flutter (A in Fig. 8) in the first mode. For larger L_x, two modes dominate (the first and the second), and so this is a coupled type of flutter (B in Fig. 8) caused by the interaction of these two modes through the aerodynamic coupling. Note that at $\theta = 0°$, spanwise modes are decoupled from each other [14,26,27], i.e., $|C_j^i| = 0$ for $j > 1$; the interaction occurs only between chordwise modes C_1^1 and C_1^2 (Fig. 11).

With an increase in θ, the aerodynamic coupling yields the interaction between spanwise modes as well (Fig. 12). The interaction of several modes leads to the appearance of additional flutter regions. Namely, Fig. 12 shows that in the region C at $\theta = 10°$ and $L_y = 600$ (Fig. 9) modes T_1^1, T_1^2, T_2^1, and T_2^2 have nonzero amplitude; i.e., all four modes and their interaction are responsible for the corresponding instability region. But still, there remain regions where either only one mode (A in Figs. 9 and 10) or two modes (B in Figs. 9 and 10) dominate.

When several spanwise eigenmodes interact with each other in region C, spanwise-traveling-wave-flutter takes place (Fig. 13). This phenomenon was not observed at zero yaw angle, where the wave could be traveling only in the streamwise direction.

For larger values of θ, the results become even more complex (Fig. 14). A sufficiently strong irregularity of the flutter boundaries exists already at large L_y. With decreasing dimensionless width,

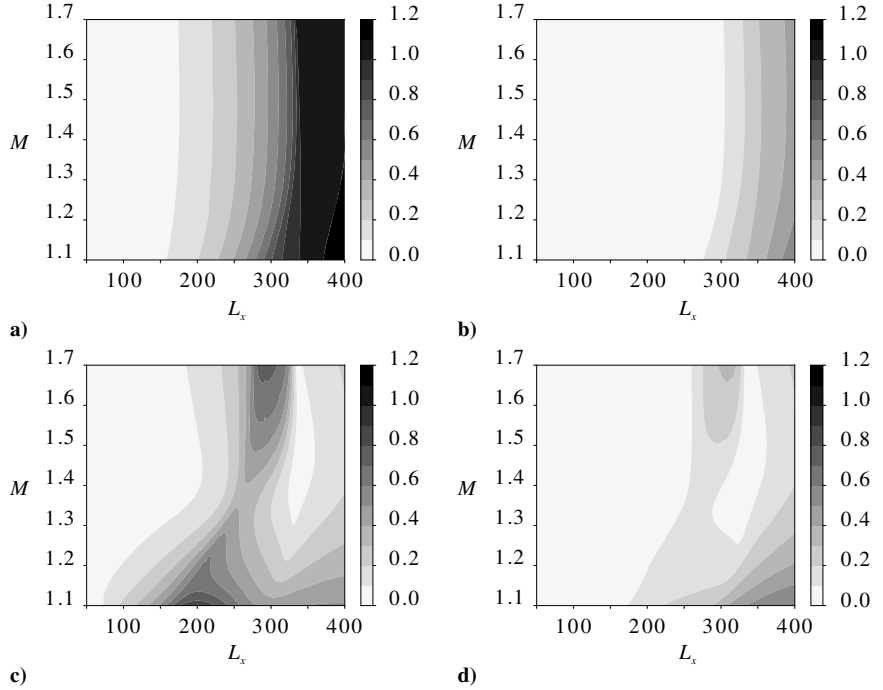

Fig. 12 Coefficients of the plate deflection expansion in natural mode shapes ($\theta = 10°$, $L_y = 600$): a) $|C_1^2|$, b) $|C_1^3|$, c) $|C_2^1|$, d) $|C_2^2|$.

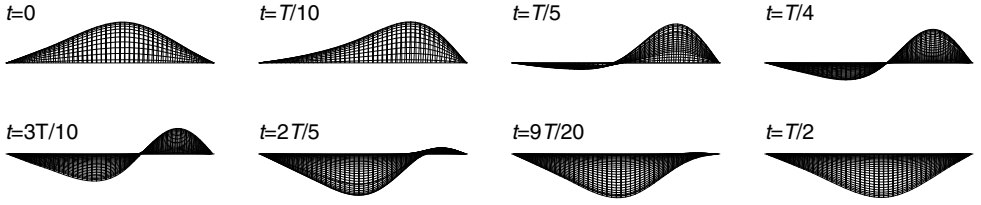

Fig. 13 Snapshots of the deformed plate shape along the oscillation half-cycle. Crossflow view (yz plane). $\theta = 15°$, $L_y = 700$, $L_x = 300$, $M = 1.46$ (region C in Fig. 10).

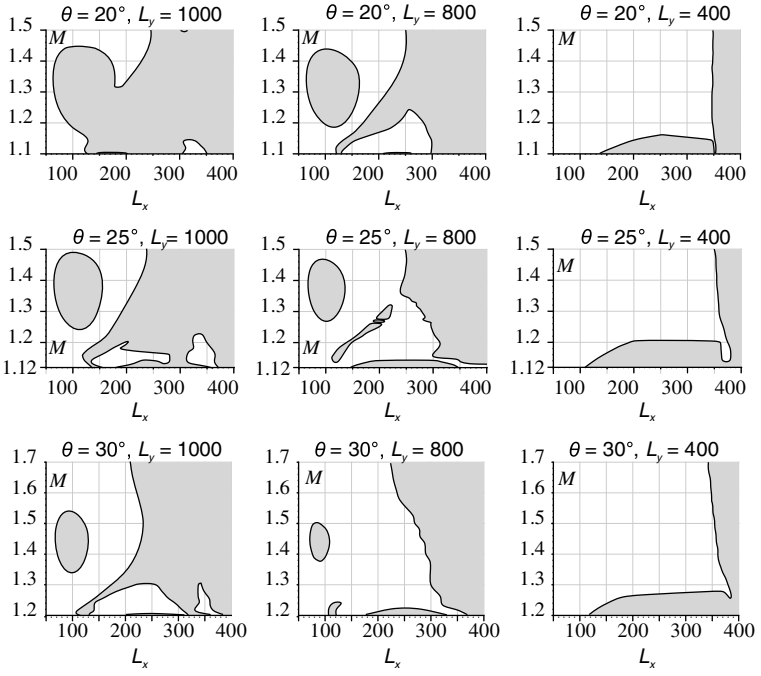

Fig. 14 Flutter boundaries for the first mode at $\theta = 20$, 25, and 30°. The instability regions are shaded with gray.

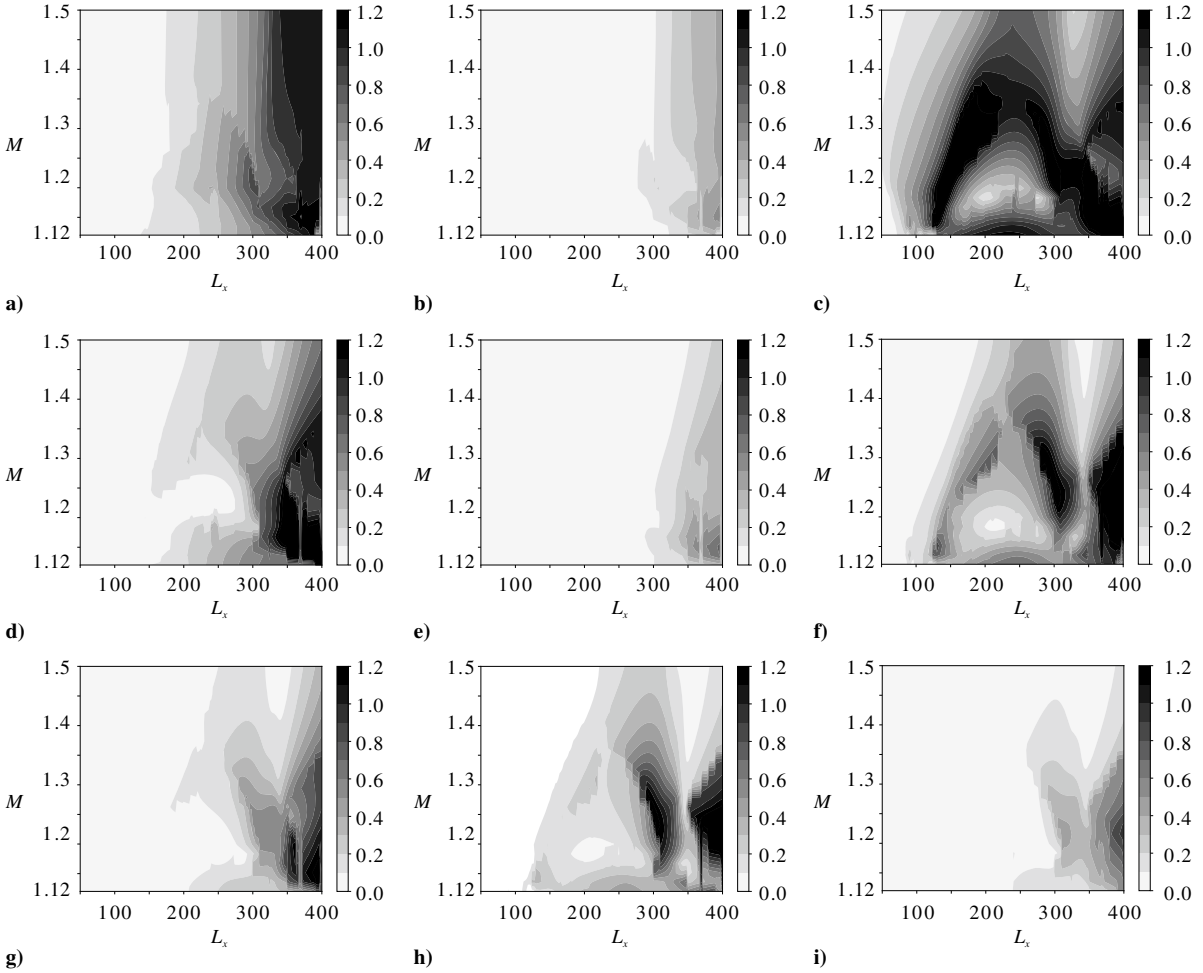

Fig. 15 Coefficients of the plate deflection expansion in natural mode shapes ($\theta = 25°$, $L_y = 800$): a) $|C_1^2|$, b) $|C_1^3|$, c) $|C_2^1|$, d) $|C_2^2|$, e) $|C_2^3|$, f) $|C_3^1|$, g) $|C_3^2|$, h) $|C_4^1|$, i) $|C_4^2|$.

isolated regions of both coupled flutter and single-mode flutter appear. In this irregularity, the interaction of multiple spanwise modes plays a key role (Fig. 15). Note that L_y at which the single-mode flutter region disappears continues to increase with increasing yaw angle: it is equal to 484, 582, and 713 at $\theta = 20$, 25, and 30°, respectively.

Thus, at a small yaw angle, the panel flutter boundaries differ little from those at a zero yaw angle, but with an increase of θ, the interactions of several modes, both chordwise and spanwise, lead to the appearance of additional regions of instability and stability. Due to the interaction of multiple modes, the boundaries loose the smoothness and become irregular.

B. Second-Mode Flutter

For the second mode, first, a comparison was made with the calculation results [24] at zero yaw angle (Fig. 16). As for the first mode, there is a good agreement between the flutter boundaries.

At small angles θ, but at slightly larger range than for the first mode, the results stay qualitatively close to the results at zero angle (Figs. 17 and 18). For sufficiently wide plates, there is a region of single-mode flutter in the second mode. It is seen that for $L_y = 1000$ and $\theta = 5°$ this region is located at $88 < L_x < 325$ and $M < 1.48$, and for $L_y = 1000$ and $\theta = 10°$ this region is located at $87 < L_x < 325$ and $M < 1.5$. With decreasing L_y, the region of instability becomes smaller. Then, at a certain value of L_y, it contracts to a point and disappears. This value of L_y increases with increasing yaw angle:

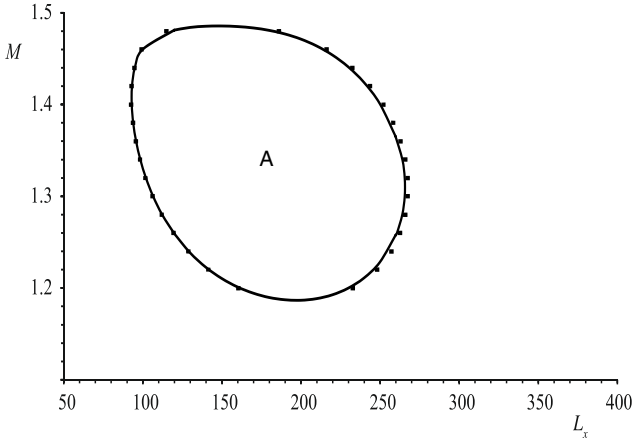

Fig. 16 Comparison of the results of the present work (points) and the those obtained by Shitov and Vedeneev [24] at zero yaw angle for the second mode and $L_y = 300$.

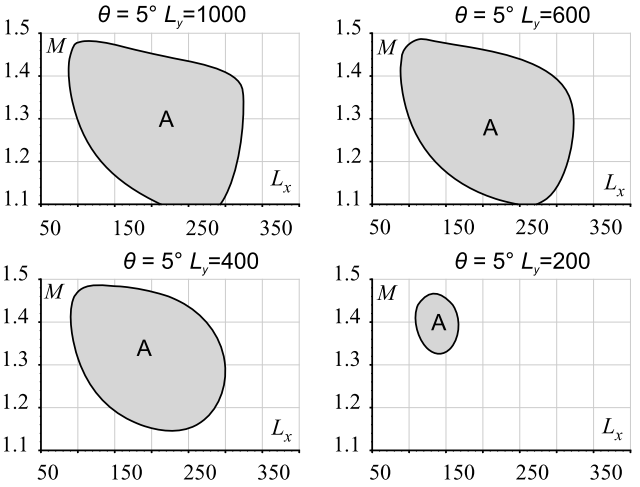

Fig. 17 Flutter boundaries for the second mode at $\theta = 5°$. The instability regions are shaded with gray.

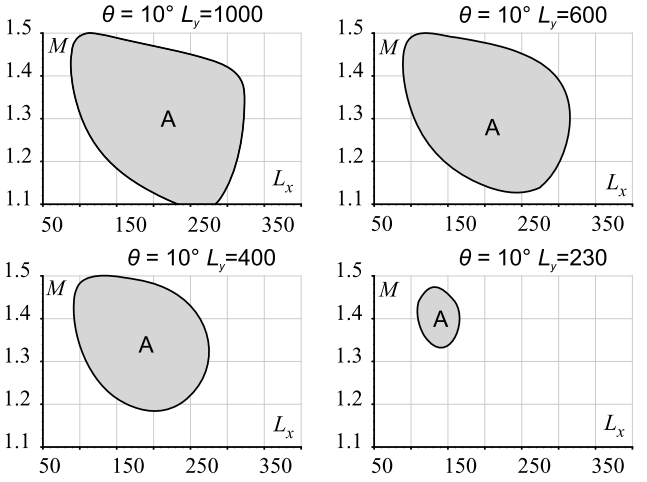

Fig. 18 Flutter boundaries for the second mode at $\theta = 10°$. The instability regions are shaded with gray.

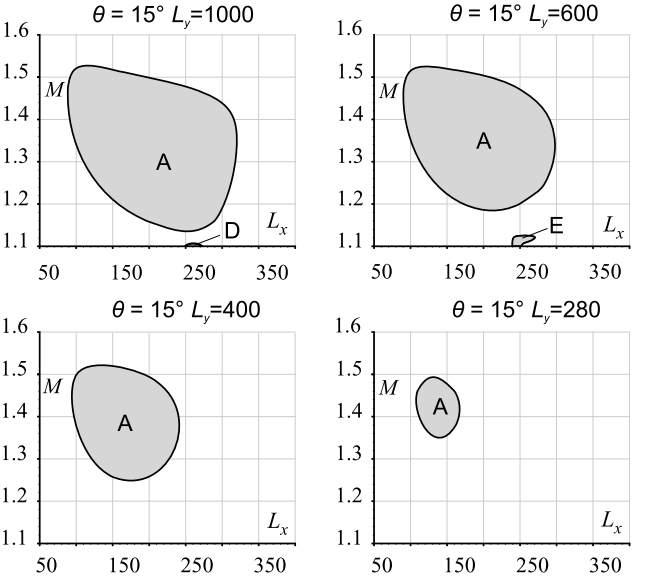

Fig. 19 Flutter boundaries for the second mode at $\theta = 15°$. The instability regions are shaded with gray.

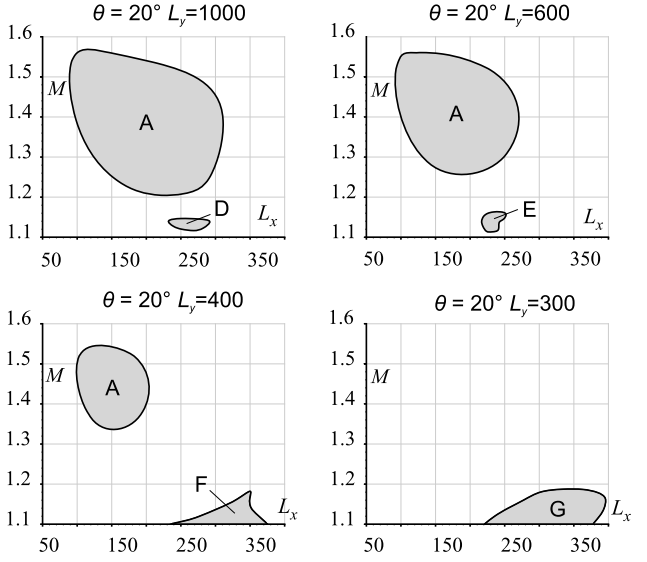

Fig. 20 Flutter boundaries for the second mode at $\theta = 20°$. The instability regions are shaded with gray.

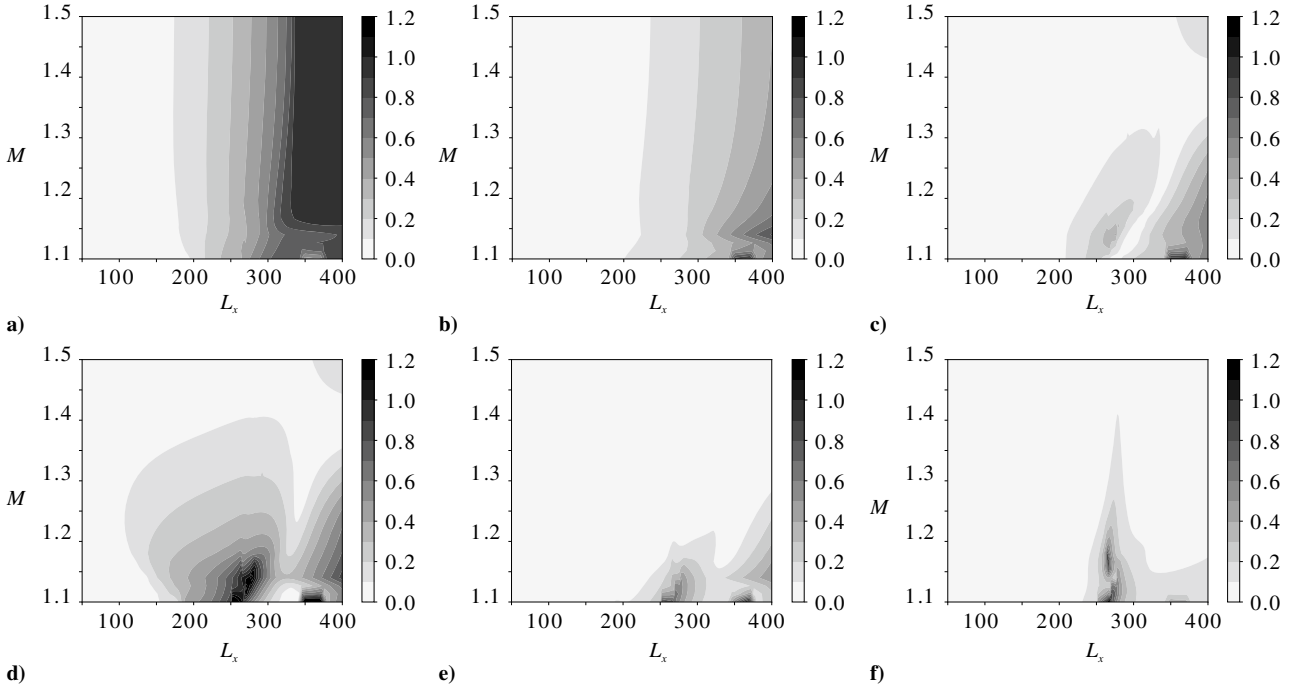

Fig. 21 Coefficients of the plate deflection expansion in natural mode shapes ($\theta = 15°$, $L_y = 600$): a) $|C_1^1|$, b) $|C_1^3|$, c) $|C_2^1|$, d) $|C_2^2|$, e) $|C_3^2|$, f) $|C_4^1|$.

$L_y = 183$ at $\theta = 5°$, $L_y = 211$ at $\theta = 10°$, $L_y = 256$ at $\theta = 15°$, and $L_y = 386$ at $\theta = 25°$.

With an increase in the yaw angle, the appearance of new regions of instability (D and E in Fig. 19, and D–G in Fig. 20) is observed. Their appearance is caused by the interaction of several plate modes, both streamwise and spanwise, which is seen from the expansion coefficients of the plate flutter mode into natural mode shapes with the condition that the second natural mode shape amplitude $C_1^2 = 1$ (Fig. 21). In all cases the single-mode flutter region (A in Figs. 19 and 20) gradually decreases in size with the decreasing plate width. With an increase in the angle, this region shifts to larger Mach numbers. For example, at $L_y = 1000$ for $\theta = 5°$ single-mode flutter appears at $1.1 \le M < 1.49$, for $\theta = 10°$ at $1.1 \le M < 1.5$, for $\theta = 15°$ at $1.13 < M < 1.53$, for $\theta = 20°$ at $1.2 < M < 1.57$, for $\theta = 25°$ at $1.28 < M < 1.63$, and for $\theta = 30°$ at $1.37 < M < 1.69$.

With a further increase in the yaw angle, the number of regions of multiple-mode flutter, caused by the interaction of several plate modes, becomes larger (Figs. 22 and 23).

Thus, at small angles, but in a somewhat wider range than for the first mode, the flutter boundary is similar to the case of a zero angle. However, at larger angles, similar to the first mode, irregular isolated regions of instability appear.

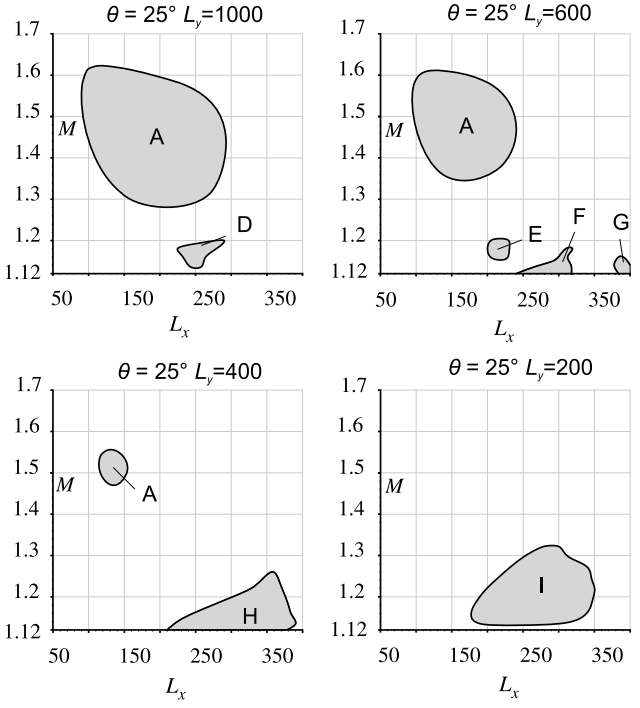

Fig. 22 Flutter boundaries for the second mode at $\theta = 25°$. The instability regions are shaded with gray.

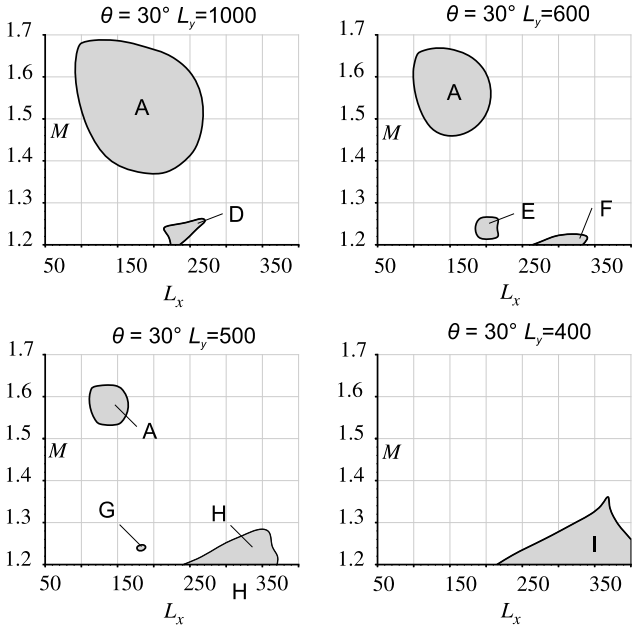

Fig. 23 Flutter boundaries for the second mode at $\theta = 30°$. The instability regions are shaded with gray.

VI. Conclusions

Using linearized potential flow theory and Bubnov–Galerkin procedure, the stability of a series of rectangular plates at a nonzero yaw angle is investigated with respect to the first and second modes.

At low yaw angles, the flutter zones are qualitatively close to those at zero angle and consist of single-mode and coupled-mode flutter regions, which are connected at large L_y, and separated at lower L_y; for sufficient low L_y the single-mode flutter region contracts to a point and disappears. With an increase in the yaw angle, the value of L_y, at which the single-mode flutter regions disappear, increases; i.e., the panel is stabilized in this sense.

An increase in the yaw angle also leads to the irregularity of the coupled-mode flutter boundary and to the formation of additional isolated regions of instability. Comparing with zero angle, these new flutter regions appear due to the interaction of two or more spanwise plate eigenmodes through the aerodynamic coupling. Due to the interaction of several modes plate oscillation has a spanwise-traveling wave form.

Note that multiple-mode flutter zones observed in this study are obtained in a linear formulation and include at least two spanwise modes. This is in contrast to multiple-mode flutter oscillations at zero yaw angle studied in previous works, where all interacting modes are streamwise, and their interaction is a purely nonlinear effect.

In terms of practical aspects, present results show that flutter analysis only at zero yaw angle is not conservative. First, yawed flow yields the shift of the primary single-mode flutter region to larger Mach numbers. Second, additional instability zones, with irregular, nonsmooth boundaries, appear unexpectedly at the parameters that are quite far from those where flutter existed at zero angle. Hence, in aeronautical applications, the case of yawed flow should be considered with care, and nonzero yaw angle should be included into the flutter model if the typical flight cycle has a significant portion of a yawed flow.

Acknowledgment

This work is supported by the Ministry of Science and Higher Education of the Russian Federation within the Program of "Supersonic" (agreement 075-15-2020-923).

References

[1] Dowell, E. H., *Aeroelasticity of Plates and Shells*, Noordhoff International Publishing, Leyden, The Netherlands, 1974, Chap. 1.

[2] Movchan, A. A., "On Oscillations of a Plate Moving in a Gas," *Prikladnaia Matematika I Mekhanika*, Vol. 20, No. 2, 1956, pp. 211–222 (in Russian).

[3] Movchan, A. A., "On Stability of a Panel Moving in a Gas," *Prikladnaia Matematika I Mekhanika*, Vol. 21, No. 2, 1957, pp. 231–243 (in Russian; translated in NASA RE 11-22-58 W, 1959).

[4] Dugundji, J., "Theoretical Considerations of Panel Flutter at High Supersonic Mach Numbers," *AIAA Journal*, Vol. 4, No. 7, 1966, pp. 1257–1266. https://doi.org/10.2514/3.3657

[5] Mei, C., Abdel-Motagaly, K., and Chen, R. R., "Review of Nonlinear Panel Flutter at Supersonic and Hypersonic Speeds," *Applied Mechanics Reviews*, Vol. 52, No. 10, 1999, pp. 321–332. https://doi.org/10.1115/1.3098919

[6] Bendiksen, O. O., and Seber, G., "Fluid–Structure Interactions with Both Structural and Fluid Nonlinearities," *Journal of Sound and Vibration*, Vol. 315, No. 3, 2008, pp. 664–684. https://doi.org/10.1016/j.jsv.2008.03.034

[7] Vedeneev, V., Guvernyuk, S., Zubkov, A., and Kolotnikov, M., "Experimental Observation of Single Mode Panel Flutter in Supersonic Gas Flow," *Journal of Fluids and Structures*, Vol. 26, No. 5, 2010, pp. 764–779. https://doi.org/10.1016/j.jfluidstructs.2010.04.004

[8] Alder, M., "Development and Validation of a Fluid–Structure Solver for Transonic Panel Flutter," *AIAA Journal*, Vol. 53, No. 12, 2015, pp. 3509–3521. https://doi.org/10.2514/1.J054013

[9] Shishaeva, A., Vedeneev, V., and Aksenov, A., "Nonlinear Single-Mode and Multi-Mode Panel Flutter Oscillations at Low Supersonic Speeds," *Journal of Fluids and Structures*, Vol. 56, July 2015, pp. 205–223. https://doi.org/10.1016/j.jfluidstructs.2015.05.005

[10] Hejranfar, K., and Azampour, M. H., "Simulation of 2D Fluid–Structure Interaction in Inviscid Compressible Flows Using a Cell-Vertex Central Difference Finite Volume Method," *Journal of Fluids and Structures*, Vol. 67, Nov. 2016, pp. 190–218. https://doi.org/10.1016/j.jfluidstructs.2016.09.009

[11] Bondarev, V., and Vedeneev, V., "Influence of the Viscous Boundary Layer Perturbations on Single-Mode Panel Flutter at Finite Reynolds Numbers," *Journal of Fluid Mechanics*, Vol. 852, Aug. 2018, pp. 578–601. https://doi.org/10.1017/jfm.2018.527

[12] Shishaeva, A., Vedeneev, V., Aksenov, A., and Sushko, G., "Transonic Panel Flutter in Accelerating or Decelerating Flow Conditions," *AIAA Journal*, Vol. 56, No. 6, 2018, pp. 997–1010. https://doi.org/10.2514/1.J056217

[13] An, X., Qi, B., Sun, W., and Deng, B., "Numerical Simulation of Nonlinear Aeroelastic Behaviors of Composite Panels in Transonic Flow," *Journal of Sound and Vibration*, Vol. 469, March 2020, Paper 115143. https://doi.org/10.1016/j.jsv.2019.115143

[14] Zhou, H., Wang, G., Mian, H. H., and Qin, M., "Fluid-Structure Coupled Analysis of Tandem 2D Elastic Panels," *Aerospace Science and Technology*, Vol. 111, April 2021, Paper 106521. https://doi.org/10.1016/j.ast.2021.106521

[15] Amabili, M., and Pellicano, F., "Nonlinear Supersonic Flutter of Circular Cylindrical Shells," *AIAA Journal*, Vol. 39, No. 4, 2001, pp. 564–573. https://doi.org/10.2514/2.1365

[16] Amabili, M., and Pellicano, F., "Multimode Approach to Nonlinear Supersonic Flutter of Imperfect Circular Cylindrical Shells," *Journal of Applied Mechanics*, Vol. 69, No. 2, 2002, pp. 117–129. https://doi.org/10.1115/1.1435366

[17] Durvasula, S., "Flutter of Clamped Skew Panels in Supersonic Flow," *Journal of Aircraft*, Vol. 8, May 1971, pp. 461–466. https://doi.org/10.2514/3.44280

[18] Abdukhakimov, F., and Vedeneev, V., "Investigation of Single-Mode Flutter of Various Form Plates at Low Supersonic Speeds," *TsAGI Science Journal*, Vol. 48, No. 1, 2017, pp. 97–110. https://doi.org/10.1615/TsAGISciJ.2017020523

[19] Mei, G., Zhang, J., and Kang, C., "Analysis of Curved Panel Flutter in Supersonic and Transonic Airflows Using a Fluid–Structure Coupling Algorithm," *Journal of Vibration and Acoustics*, Vol. 139, No. 4, 2017, Paper 041004. https://doi.org/10.1115/1.4036103

[20] Bhatia, M., and Beran, P., "Influence of Aerodynamic Nonlinearity Due to Static Panel-Curvature on Flutter of Panels at Transonic and Low Supersonic Mach Numbers," *Journal of Fluids and Structures*, Vol. 81, Aug. 2018, pp. 574–597. https://doi.org/10.1016/j.jfluidstructs.2018.05.015

[21] Abdel-Motaglay, K., Chen, R., and Mei, C., "Nonlinear Flutter of Composite Panels Under Yawed Supersonic Flow Using Finite Elements," *AIAA Journal*, Vol. 37, No. 9, 1999, pp. 1025–1032. https://doi.org/10.2514/2.818

[22] Guo, X., and Mei, C., "Using Aeroelastic Modes for Nonlinear Panel Flutter At Arbitrary Supersonic Yawed Angle," *AIAA Journal*, Vol. 41, No. 2, 2003, pp. 272–279. https://doi.org/10.2514/2.1940

[23] Abdel-Motagaly, K., Guo, X., and Mei, C., "Active Control of Nonlinear Panel Flutter under Yawed Supersonic Flow," *AIAA Journal*, Vol. 43, No. 2, 2005, pp. 671–680. https://doi.org/10.2514/1.13840

[24] Shitov, S., and Vedeneev, V., "Flutter of Rectangular Simply Supported Plates at Low Supersonic Speeds," *Journal of Fluids and Structures*, Vol. 69, Feb. 2017, pp. 154–173. https://doi.org/10.1016/j.jfluidstructs.2016.11.014

[25] Miles, J. W., *The Potential Theory of Unsteady Supersonic Flow*, Cambridge Univ. Press, Cambridge, England, U.K., 1959, Chap. 5.

[26] Vedeneev, V. V., "Nonlinear High-Frequency Flutter of a Plate," *Fluid Dynamics*, Vol. 41, March 2007, pp. 858–868. https://doi.org/10.1007/s10697-006-0046-7

[27] Vedeneev, V. V., "Limit Oscillatory Cycles in the Single Mode Flutter of a Plate," *Journal of Applied Mathematics and Mechanics*, Vol. 77, No. 3, 2013, pp. 257–267.

S. Shin
Associate Editor